Surface & Coatings Technology 396 (2020) 125950

Contents lists available at ScienceDirect

Surface & Coatings Technology

journal homepage: www.elsevier.com/locate/surfcoat

Thermal barrier coatings with novel architectures for diesel engine applications

Wellington Uczak de Goes[a,*], Nicolaie Markocsan[a], Mohit Gupta[a], Robert Vaßen[b], Taishi Matsushita[c], Kseniya Illkova[d]

[a] University West, Trollhättan, Sweden
[b] Forschungszentrum Jülich, Germany
[c] Jönköping University, Sweden
[d] Institute of Plasma Physics, Prague, Czech Republic

ARTICLE INFO

Keywords:
Suspension plasma spray
Diesel engine
Sealing coating
Yttria stabilized zirconia
Gadolinium zirconate

ABSTRACT

The increased demands for higher efficiency and environmentally friendly diesel engines have led to a continuous search for new coating processing routes and new ceramic materials that can provide the required properties when applied on engine components such as pistons and exhaust manifolds. Although successful in gas turbine applications, thermal barrier coatings (TBCs) produced by suspension plasma spraying (SPS) processes have not been employed so far in the automotive industry. This work aims to achieve a better understanding of the role of thermal conductivity and thermal effusivity on the durability of SPS TBCs applied to pistons of diesel engines. Three different coating architectures were considered for this study. The first architecture was yttria-stabilized zirconia (YSZ) lamellar top coat deposited by APS (Atmospheric Plasma Spray) and used as a reference sample in this study. The second architecture was a columnar SPS top coat of either YSZ or gadolinium zirconate (GZO) while the third architecture was an SPS columnar top coat, "sealed" with a dense sealing layer deposited on the top coat. Two types of sealing layers were used, a metallic (M) or a ceramic thermal spray layer (C). Laser Flash Analysis (LFA) was used to determine the thermal conductivity and thermal effusivity of the coatings. Two different thermal cyclic tests were used to test the TBCs behavior under cyclic thermal loads. Microstructure analysis before and after the thermal cyclic tests were performed using SEM in different microstructures and materials. The thermal cyclic test results were correlated with coatings microstructure and thermophysical properties. It was observed that the columnar coatings produced by SPS had an enhanced service life in the thermal cyclic tests as compared to the APS coatings.

1. Introduction

The standing increase in greenhouse gas emissions in the past decades has led to unprecedented global warming. To fight this trend and reduce the catastrophic effects, a new climate regulation was released in Sweden on January 1st, 2018 that sets ambitious goals for reducing climate impacting emissions, e.g., net-zero emissions by 2045, which is quite a milestone since it represents an 85% reduction compared to emissions in 1990 [1]. In terms of road traffic emissions, according to the Swedish Transport Administration's Annual Report for 2017, approximately 95% of greenhouse gas emissions originate from domestic transport, from which a majority of the discharge is from cars and trucks. Thus, to achieve the goal of net-zero emissions by 2045, amplified and conjugated R&D efforts should focus on improvements in internal combustion engines or alternative solutions [2].

Significant advancements in internal combustion engine technology have been accomplished over time, with many technical refinements for improving efficiency, including variable valve timing, direct fuel injection, and start-stop systems. Lightweight materials have also improved the efficiency of the engines, but further gains in this specific area, are becoming harder to achieve. Based on the experiences from the aerospace industry, thermal barrier coatings (TBCs) have been explored and have shown great promise to improve the efficiency of internal combustion engines [3].

Thermal barrier coatings for diesel engines have been studied in the last 30 years, and numerous methods and layer materials have been investigated. The application challenge resides on the different operating conditions in gas turbines and diesel engines. In gas turbines,

* Corresponding author.
E-mail address: wellington.uczak-de-goes@hv.se (W. Uczak de Goes).

https://doi.org/10.1016/j.surfcoat.2020.125950
Received 19 December 2019; Received in revised form 6 May 2020; Accepted 19 May 2020
Available online 25 May 2020

there is a high and a continuous service temperature combined with constant pressure, but in diesel engines, there is a lower and oscillating service temperature, with a cycle frequency in normal conditions around 400 cycles per minute. Thus, the coatings are exposed to a much larger number of heat pulses and oscillating pressures than in gas turbines [4]. The effect of the features in the coating influence the combustion cycle, such as the porosity that impacts the combustion cycle due to the fuel entrapment into the pores, causing a prolonged combustion [5]. In addition, the thermal insulation effect of the coatings leads to a lower volumetric efficiency. As the coatings (combustion chamber walls) get hotter, the amount of air admitted in the combustion chamber is reduced and leads to the lower volumetric efficiency [5–7]. The effect of the combustion fuels and gases on the coatings may pose a challenge as well, e.g., the coatings need to cope with the oxidative and corrosive environment due to the contaminants that can be found in the fuels [4,5,8,9].

The first approach involved coatings of yttria-stabilized zirconia (YSZ) and mullite, meant to keep the heat inside the combustion chamber, creating a low heat rejection engine (LHRE). In theory, this would allow the engine to operate at a higher temperature with reduced external cooling, increasing the overall engine efficiency. Some conclusions from this work were that for both coatings, the efficiency was increased, the combustion cycle was prolonged, and the volumetric efficiency decreased [6].

Modi [8] coated the combustion chamber walls, piston crown faces, valves, top surface of the cylinder head, and liners with YSZ creating an LHRE and studying the effect of the insulated heat transfer surfaces on the diesel engine. Partially stabilized zirconia was selected because of its wear resistance, low thermal conductivity, high thermal shock resistance, and high melting point. The results of the coated engine showed an increase in the wall temperature in the same way as Beardsley et al. [5], which led to a decrease in the volumetric efficiency of the engine. However, increased boost pressure from the turbocharger could be used to solve this situation. The overall performance of the coated engine was improved compared to the standard engine.

Kosaka et al. [10] investigated the concept now called as temperature swing heat insulation, which similarly to the coatings used in the study by Osawa et al. [11] employed a porous coating that could follow the transient gas temperature, i.e., a coating with low heat conductivity and low heat capacity. This concept can work because, in theory, if the thermal energy is kept inside of the combustion chamber combined with the fact that the volumetric efficiency would not be affected by the heated walls, there would be higher engine efficiency.

Kawaguchi et al. [12] applied the concept presented in [8,9] using an anodized aluminum alloy piston with a 70 μm thick porous alumina columnar structure. Due to the porous and columnar microstructure, the penetration of burning gases into the pores needed to be addressed, as in [8], a sealing layer was applied using perhydropolysilazane. This sealing layer had a few microns thickness over the porous layer giving the protection against the cylinder gas penetration into the pores.

To date, the focus of most research has been on the classic atmospheric plasma spray (APS), a process that uses a plasma torch and a dry powder feedstock to produce coatings with a lamellar microstructure [5,6,8]. This study was conducted using the relatively newly developed thermal spray process, suspension plasma spray (SPS), wherein a plasma torch is used with submicron-sized feedstocks suspended in a liquid. This novel technique provides a microstructure that resembles the coating proposed in [10] (i.e., columnar) and offers a mix of features with outstanding characteristics. SPS has not been studied so far for diesel engine applications, excepting the work presented in [13]. SPS can produce porous coatings, comparable with the APS coatings, and columnar coatings similar to the electron beam physical vapor deposition (EB-PVD); coatings used traditionally in gas turbine applications, creating a TBC with high strain tolerance and low thermal conductivity, appropriate to diesel engines conditions [13–15].

The purpose of this study was to employ suspension plasma spraying (SPS) to produce various coatings with columnar microstructure and to assess the possibility of increasing the efficiency of diesel engines with this type of coatings. Both coatings with a sealing layer and without a sealing layer were investigated in this study. The targeted industrial application of the coatings investigated in this study was diesel engines for heavy-duty vehicles, but the results can be applied to other engines.

2. Material and methods

2.1. Sample preparation

Thermal barrier coatings are multi-layered systems that typically have a first intermetallic layer (bond coat) that guarantees adhesion and protects the metal substrate from oxidation and corrosion. Over the bond coat, a top coat of a ceramic material with low thermal conductivity is applied to provide the thermal gradient needed for higher temperature applications. Herein, a sealing layer over the top coat was also applied to prevent fuel and combustion gases entering the pores of the ceramic coating, which may cause engine performance losses [5,6,8,11,13–15]. The sealing layers used were the metallic (M) and the ceramic thermal spray layer (C).

In this study, eight different samples were sprayed with three architectures, as schematically shown in Fig. 1 and described in Table 1. The substrate used in this study was, a commercial-grade medium carbon micro-alloyed with vanadium steel (38MnSiVS5), in the form of buttons (25.4 mm diameter × 6 mm thickness). The chemical composition of the substrate is similar to the material used in pistons for diesel engines in heavy-duty vehicles. The first architecture, comprising of a lamellar APS bond coat and top coat, was used as a reference sample. The reason for considering this sample as a reference is that

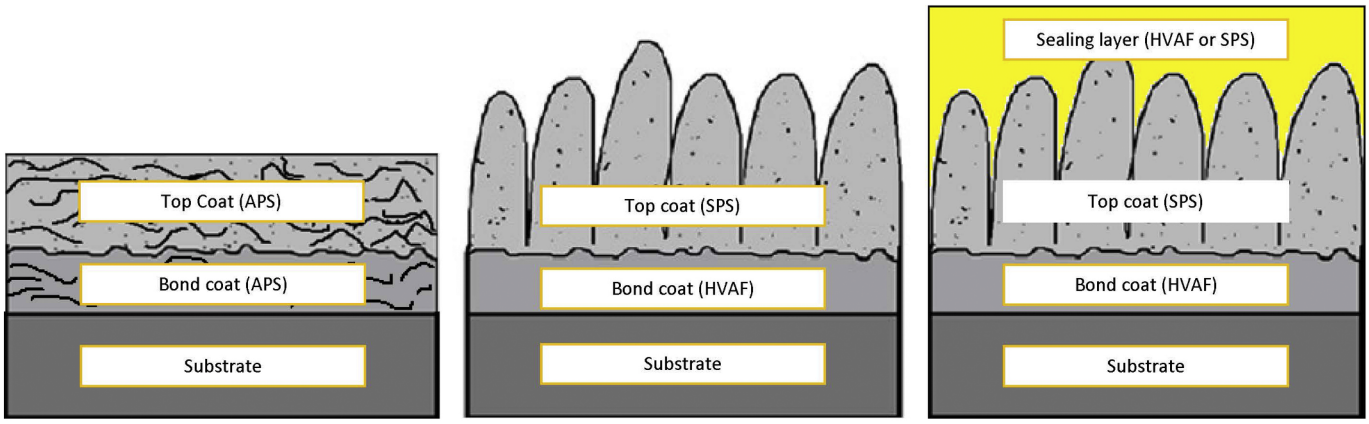

Fig. 1. Different coating architectures.

Table 1
Abbreviation and details of the TBCs.

Abbreviation	Bond coat		Top coat		Sealing layer	
	Process	Thickness, μm	Process	Thickness, μm	Process	Thickness, μm
APS	APS	108 ± 12	APS	272 ± 11	No sealing	–
SPS YSZ	HVAF	125 ± 13	SPS	250 ± 10	No sealing	–
SPS YSZ T	HVAF	130 ± 7	SPS	424 ± 8	No sealing	–
SPS GZO	HVAF	134 ± 10	SPS	217 ± 9	No sealing	–
SPS YSZ P-M	HVAF	139 ± 9	SPS	231 ± 11	HVAF	56 ± 8
SPS YSZ-M	HVAF	133 ± 7	SPS	215 ± 9	HVAF	40 ± 10
SPS GZO-M	HVAF	124 ± 8	SPS	243 ± 12	HVAF	50 ± 8
SPS GZO-C	HVAF	128 ± 12	SPS	208 ± 11	SPS	39 ± 8

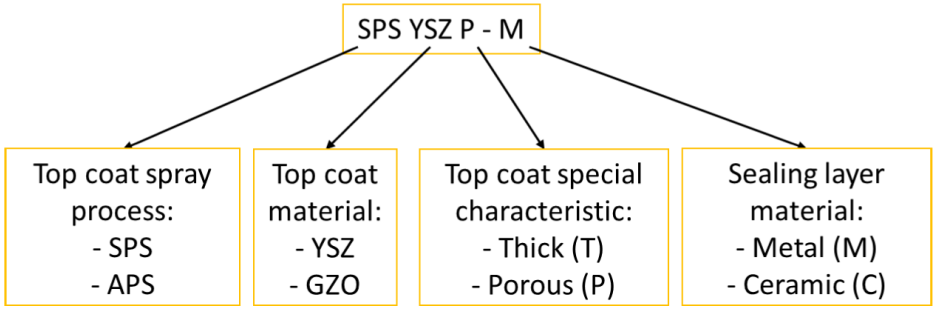

such type of coating has been mostly studied for diesel engine applications [5,6,8,13]. The second architecture was composed of a dense HVAF bond coat and a columnar SPS top coat. For the top coating, different compositions (YSZ or GZO) and different top coat thicknesses were investigated (Table 1). The third architecture consisted of a dense HVAF bond coat, a columnar SPS top coat with different compositions (YSZ or GZO) and different porosities, and a sealing layer over the top coat. Two types of sealing layers were investigated in this study, a metallic layer sprayed by HVAF and a ceramic layer sprayed by SPS (Table 1).

The F4-MB plasma spray gun from Oerlikon Metco was used to spray the APS coating for the reference sample using a feedstock powder of NiCoCrAlY (AMPERIT 410) for the bond coat and a feedstock powder of YSZ (METCO 204 B-NS) for the top coat. For the HVAF process, the M3 gun from Uniquecoat Technologies was used with a NiCoCrAlY feedstock (AMDRY 386) for depositing the bond coats of the rest of the samples as well as the metallic sealing layer. The Axial III torch, a plasma torch from Mettech Corp., equipped with a Nanofeed 350 suspension feed system, was used to spray the SPS top coats and the ceramic sealing layer. For the top coat, two suspensions, one of 8YSZ and the other one of GZO, with 25 wt% solid load in ethanol (Treibacher Industrie AG), were used. For the ceramic sealing layer, a GZO suspension with a solid load of 40 wt% in water (Treibacher Industrie AG) was employed.

The measurement of the coating thickness was done on micrographs of the cross-sectioned coatings, using a light optical microscope, BX60M from OLYMPUS. The average of ten measurements was taken as the final value.

2.2. Metallographic preparation

For the sample preparation for microstructure analysis, a specific procedure was used to preserve the sample microstructure. First, the samples were cold mounted using a low viscosity epoxy resin to fill all the pores with resin to prevent pull-outs and cracks. The following step involved the cutting of the mounted samples with an abrasive cutting disc. Finally, the samples were cold mounted again but with a high viscosity resin. The last part of the preparation consisted of sequential semi-automatic grinding and polishing steps using the Buehler Power Pro 5000 instrument.

2.3. Porosity measurement

Image analysis of scanning electron microscopy (SEM) microstructure images was used to measure the porosity of the coatings. Single magnification (500×) was selected for the first architecture samples due to the greater pore size of the APS coating. For the second and third architectures due to the large variation in the pore sizes on the SPS coating, a single magnification cannot cover the entire range of pore sizes. As described in detail by Ganvir et al. [16], two magnifications, one low (500×) and one high (5000×), can accurately detect the entire range of the pores existing in SPS coatings. ImageJ, a program developed at the National Institute of Health, USA, was used to evaluate the pores. Coarse porosity, i.e., pores with an area on the cross-section pictures larger than 2 μm^2, was analyzed on low magnification images (500×). It was essential to ensure that in the third type of architecture, both the top coat and the sealing layer were captured in the low magnification image. Fine porosity, i.e., pores with an area on the cross-section pictures, smaller than 2 μm^2, was analyzed on high magnification images (5000×). For the samples with a sealing layer, pictures at high magnification were taken separately for the top coat and sealing layers. The accuracy of the porosity was assured with ten images taken for each layer, along with the entire coating at high and low magnifications.

For the first architecture, the APS sample, the total porosity was calculated based on the single image porosity. For the second architecture, the unsealed SPS samples, the total porosity was the sum of the average coarse porosity and average fine porosity. For the third architecture, the sealed SPS samples, a different routine was followed considering the coarse and fine porosity as schematically shown in Fig. 2, and the final porosity determined in Eq. (1). First, the average coarse porosity was calculated for the top coat and sealing layer. In the next step, the fine porosity was calculated using the rule of mixtures to ensure that the top coating and sealing layer porosities were taken into consideration.

$$\text{Third architecture top coated porosity} = \text{Cpst} + \left(\left(\frac{\text{Tth}}{(\text{Tth} + \text{Sth})} * \text{Fpt}\right) + \left(\frac{\text{Sth}}{(\text{Tth} + \text{Sth})} * \text{Fps}\right)\right) \quad (1)$$

where Cpst (Coarse porosity), Tth (Top coat thickness), Sth (Sealing

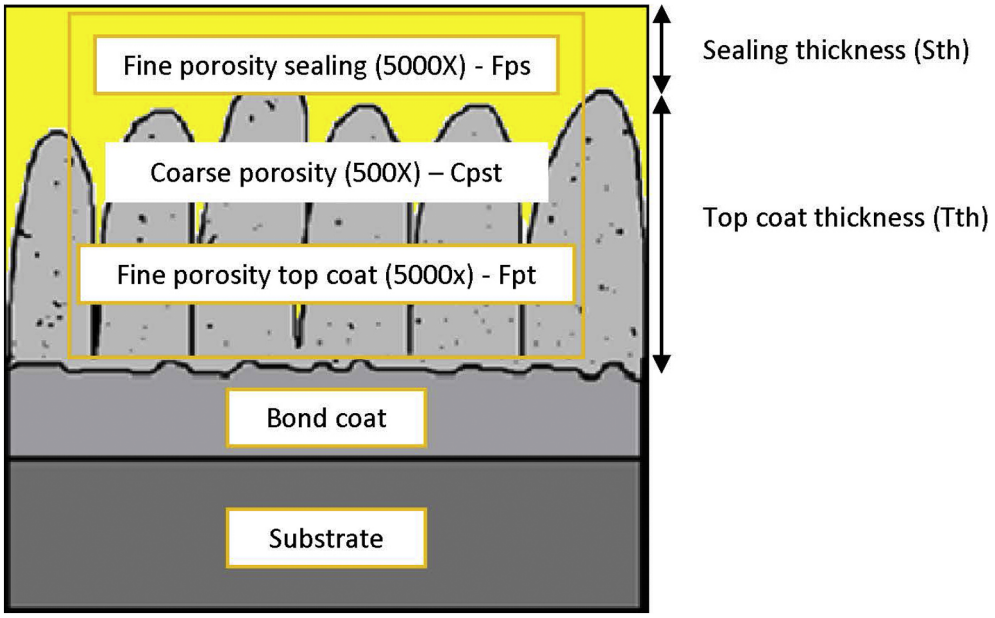

Fig. 2. Schematic of the porosity for the third architecture top coated samples.

layer thickness), Fpt (Fine porosity top coat), and Fps (Fine porosity sealing).

2.4. Thermal diffusivity

The thermal diffusivity was measured using an LFA 1000 Laser Flash apparatus from Linseis thermal analysis (IPP, Czech Republic). The sample was first covered on both sides with a thin layer of graphite to improve the absorption and emission properties. Afterward, the coated sample was placed on a sample holder that automatically guided the sample into a furnace for the measurement.

The measurement procedure for thermal diffusivity can be divided into several steps. First, the sample is heated in a furnace to the desired temperature (25–700 °C). After a constant temperature is reached, a laser of known pulse irradiates the back of the sample, increasing the temperature at the rear side of the sample. Subsequently, the temperature increase of the coating surface is recorded using a high-speed IR detector. Based on the time required for the top surface temperature of the sample to reach half of the maximum temperature increase $t_{0,5}$ [s], the thermal diffusivity α [m^2/s] can be calculated using Eq. (2) while considering the coating thickness d [m].

$$\alpha = \frac{(0.1388 \cdot d^2)}{t_{0,5}} \tag{2}$$

It should be noted that in the case of the third architecture, the top and sealing layers are considered as a single layer, and the other layers, bond coat, and substrate were separately measured previously. In addition, the measurement was performed, assuming that in the time when the heat passes within the sample, no heat resistance between layers occurred.

2.5. Thermal conductivity

Thermal conductivity was determined based on the thermal diffusivity measurements (Section 2.4) at different temperatures, using Eq. (3).

$$\lambda = \alpha \cdot \rho \cdot c_P \tag{3}$$

where λ [W/(m·K)] is the thermal conductivity, α [m^2/s] is the thermal diffusivity, ρ [g/m^3] is the density, c_P [J/(kg·K)] is the specific heat capacity of the coating. The density is a required parameter and was calculated using Eq. (4) based on the fully dense YSZ and GZO coatings and the porosity calculated in Section 2.3.

$$\rho = \left(\frac{100 - \text{total porosity}(\%)}{100}\right) * (\text{density of the fully dense coating}) \tag{4}$$

The density of the fully dense coating was assumed to be temperature independent and taken form literature as 6.1 g/cm^3 for the YSZ and 6.32 g/cm^3 for the GZO coating [17]. The specific heat capacity was used from previous differential scanning calorimetry measurements done by authors and reported in [17].

2.6. Thermal effusivity

As discussed in Appendix A, thermal effusivity (*e*) measures the ability of the material to exchange heat with the surroundings. Thermal effusivity calculated in Eq. (5) can be a more appropriate thermal property to evaluate coatings for automotive use. Because the heat conduction rate (thermal conductivity) and the rate of temperature change when this material is heated (density x specific heat capacity) are distinctly considered, giving in this way the entire perspective of the thermal energy going through the sample.

$$e = \sqrt{\lambda \cdot \rho \cdot c_P} \tag{5}$$

2.7. Coating testing

The lifetime of the coatings investigated in this study was estimated using a combination of two tests, a simplified and accelerated oven test, the thermal cyclic fatigue (TCF), with a low heat cycle shown during the start/stop of the engine. This test was combined with a flame rig test assessing the high heat cycle presented during combustion and the subsequent cooling of the surfaces.

2.7.1. Thermal cyclic fatigue test

Based on the conditions in the diesel engine, the samples were heated to 700 °C in a specially designed computer-controlled furnace composed of two chambers. In the first chamber, the samples were heated to 700 °C for 1 h and subsequently moved to the second chamber where a high-resolution camera captured images, and the samples were cooled to room temperature in 10 min using compressed air.

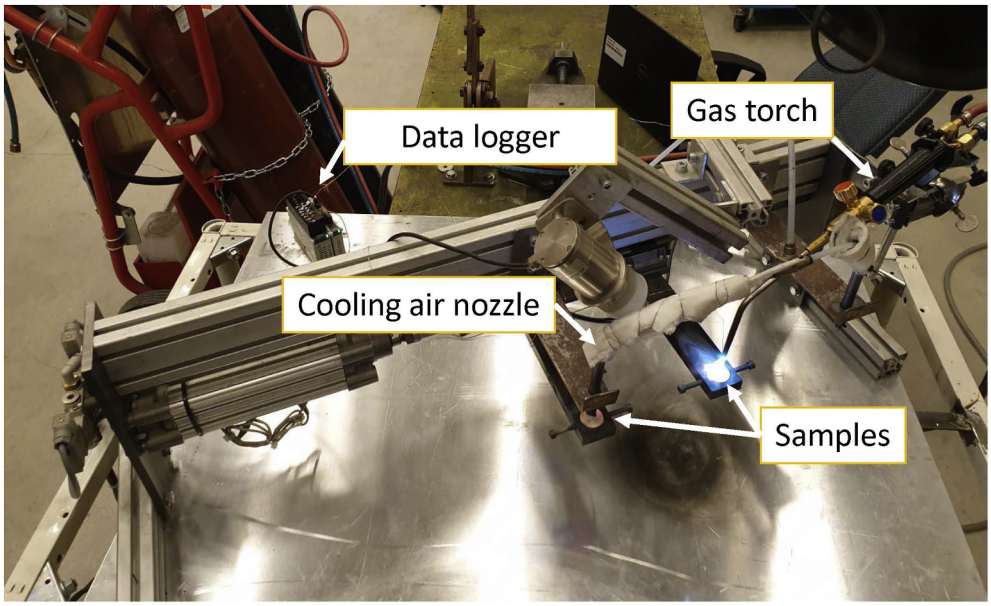

Fig. 3. Flame rig test.

Two analysis points of the test were defined to compare the effects of the test on the samples, 600, and 1000 cycles. Three samples from each set of coatings were subjected to TCF. The tested samples were cold mounted in epoxy resin, prepared, and analyzed via SEM.

2.7.2. Flame rig test

To complement the TCF tests, a flame rig test, Fig. 3, was designed and performed in collaboration with Jönköping University, Sweden. For this test, two samples from each set of the coatings were used.

The equipment consists of two sample holders mounted on a frame that can move transversally, an oxy-acetylene flame torch that is used for heating the samples from the top side, and two cooling nozzles symmetrically distributed to the flame torch for cooling the samples with compressed air, as shown in Fig. 3. To perform the test, the two samples are placed in the sample holders and cyclically moved from the flame torch to one of the cooling nozzles, depending on which side of the torch the sample is, and keeping the same cooling/heating time for all tested samples. Therefore, while one sample is heated for 6 s from the top using an oxyacetylene flame up to a temperature of approximately 700 °C, the second sample is cooled with compressed air to a temperature of approximately 600 °C. In the next step, the sample that was heated up moves to the cooling nozzle (situated on the other side of the torch) while the sample that was cooled moves to the torch for heating, completing thus a heating-cooling cycle [18].

The temperature change of the coating was measured using a K-type thermocouple installed on the side of the sample and logged every 100 ms using a Keyence NR-H7W instrument. The oxy-acetylene torch nozzle used for this test was operated at a gas flow of 315 L/h. Monitoring the “cleanness” of the torch was essential because the oxyacetylene burning process can form soot on the tip of the torch, which in turn affects the shape of the flame and hence the heat distribution on the surface of the sample. Cleaning of the torch was performed after every 500 cycles with pressurized air.

The established failure criteria adopted was 10% detachment of the coating. The failure of the samples was investigated both visually and in cross-section by SEM microscopy.

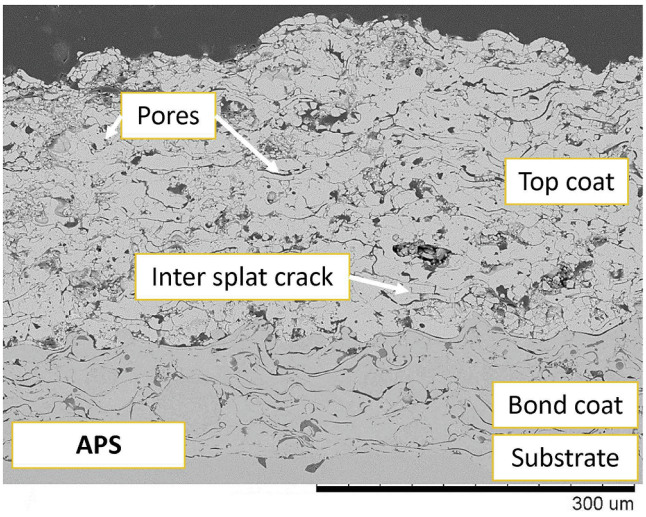

Fig. 4. APS microstructure.

3. Results

3.1. Microstructure

Figs. 4–8 show the microstructure of the coatings summarized in Table 1. Fig. 4 presents the first architecture, the APS sample, which was used as a reference sample in this study, with the typical lamellar microstructure formed from the consecutive impact and solidification of the accelerated droplets on the substrate as shown in previous studies [5,6,8,13,19]. Fig. 5 shows the cross-section of SPS YSZ and SPS YSZ T samples from the second architecture. A typical columnar microstructure was observed due to the SPS coating formation with smaller droplets, compared to the APS coating, that have their momentum influenced by the plasma plume with columns originating from the asperities of the bond coat, and column gaps that formed between the built-up columns [13,20]. Pores also can be observed in both bond coats produced by APS and HVAF but a small number of pores in the HVAF coatings. This lower porosity of the HVAF is due to the spray process that accelerates the particles to high velocities combined with the flame

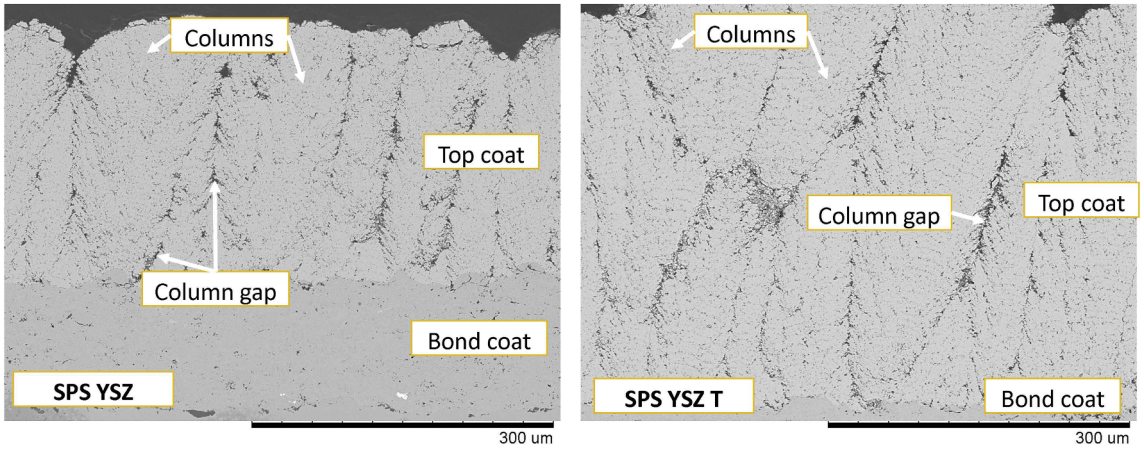

Fig. 5. Comparison of coatings microstructure SPS YSZ and SPS YSZ T.

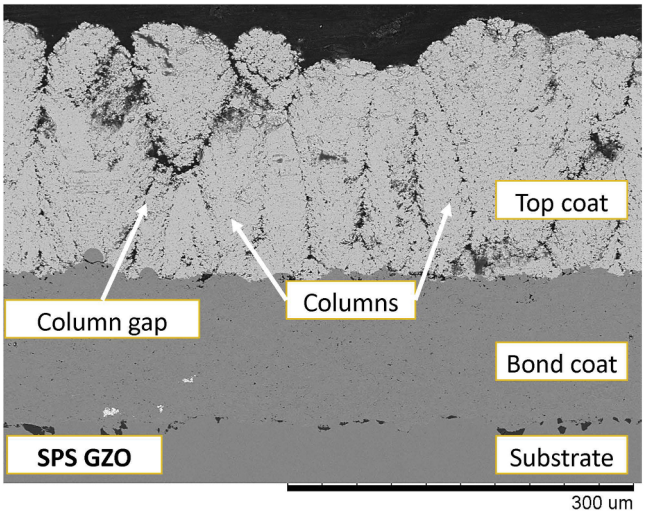

Fig. 6. Coating microstructure SPS GZO.

temperature resulting in dense coatings with reduced porosity [21].

The cross-section microstructure of an additional second architecture is shown in Fig. 6 with the SPS GZO sample. The GZO coating revealed a columnar top coat microstructure with columns and column gaps and a bond coat with low porosity, just as the SPS YSZ and SPS YSZ T coatings presented in Fig. 5.

Fig. 7 shows the cross-section of the third architecture with the SPS YSZ-M and the SPS YSZ P-M samples, displaying a similar columnar top coat microstructure and dense bond coat, as shown in Fig. 5. The porosity was higher in the SPS YSZ P-M sample due to different spraying parameters that were used to produce the top coat. The metallic sealing layer has a microstructure similar to the bond coat with a few pores and exhibits excellent coverage of the ceramic coating surface in both samples (SPS YSZ-M and SPS YSZ P-M).

Fig. 8 shows the cross-section of the remaining third architecture with the SPS GZO-M and SPS GZO-C samples. In both images, the columnar microstructure of the top coat is evident with columns rising from the asperities of the dense bond coat and distinct column gaps between the columns, like in the microstructure of the SPS GZO sample shown in Fig. 6. The metallic sealing layer presented a lower volume of pores than the ceramic sealing layer, but both sealing layers covered well all the asperities of the ceramic top coat.

3.2. Porosity

The porosity results of the samples are presented as follows, the first and second architecture samples in Fig. 9, and the third architecture samples in Fig. 10.

Fig. 9 presents a comparison between the porosity of the first and second architecture samples accordingly to the type of pores. The first architecture, the APS sample, did not exhibit small pores due to the larger particle size of the feedstock powder, and it was categorized in one porosity group. For the second architecture, two different pore groups were categorized, as explained in Section 2.3, fine and coarse porosity. The total porosity is relatively similar, the lowest porosity was found for coatings prepared via APS followed by the SPS YSZ and SPS YSZ T coatings and the highest for coarse, fine, and total porosity the

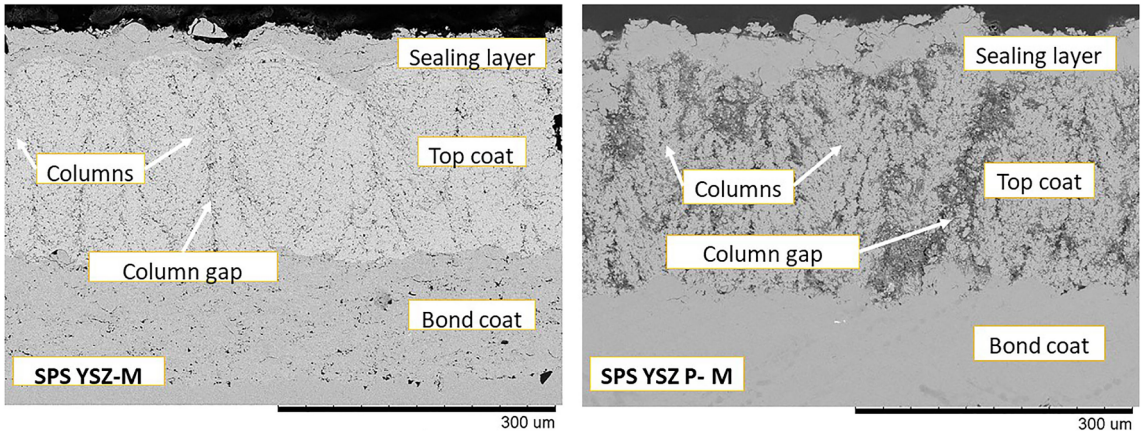

Fig. 7. Comparison of coatings microstructure SPS YSZ-M and SPS YSZ P-M.

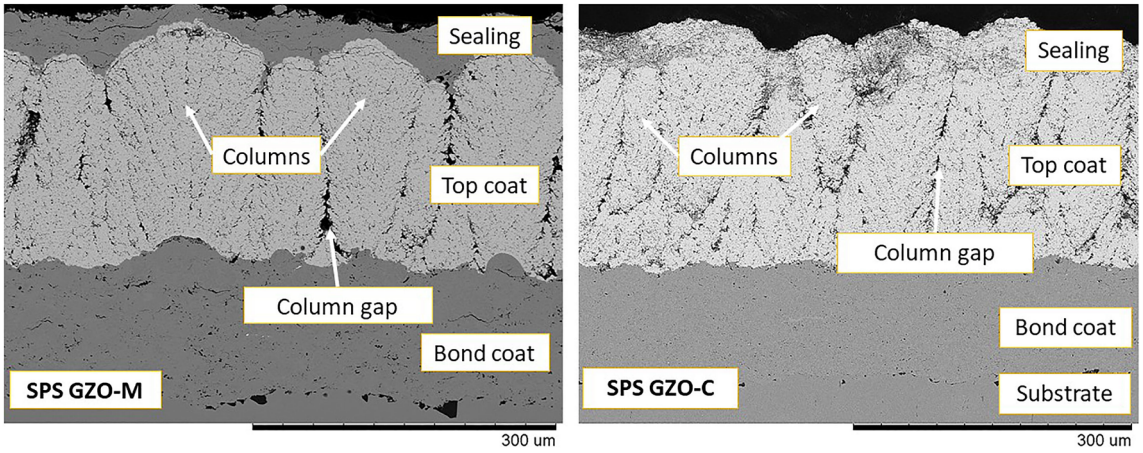

Fig. 8. Comparison of coatings microstructure SPS GZO-M and SPS GZO-C.

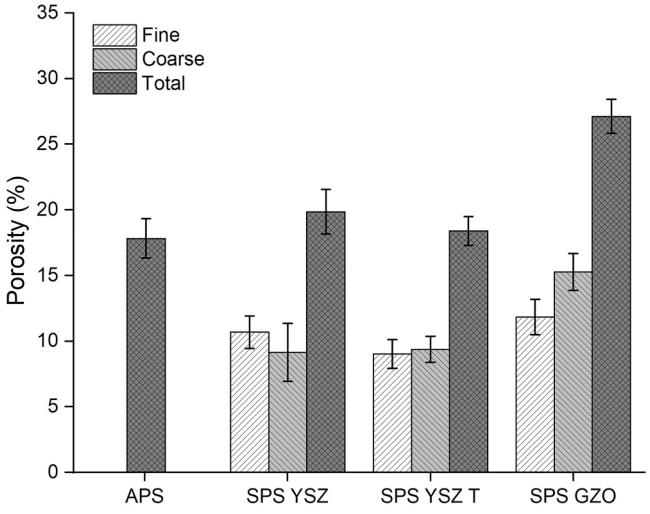

Fig. 9. Porosity content of the first and second architecture of top coated samples.

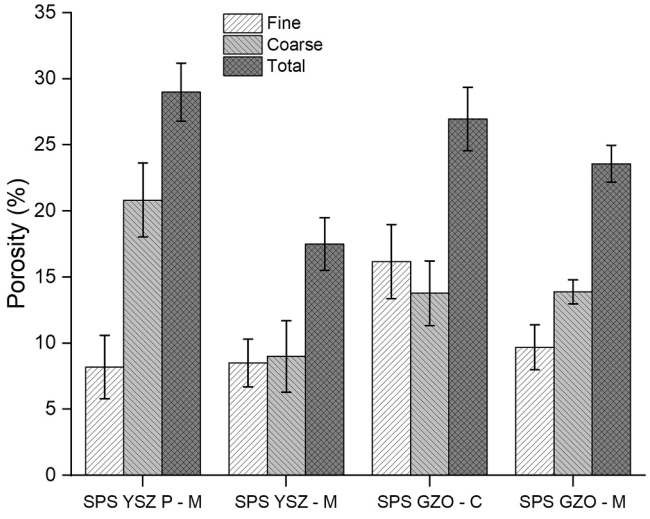

Fig. 10. Porosity content of the third architecture of top coated samples.

SPS GZO sample.

The porosity of the third architecture samples is shown in Fig. 10. The contribution of the porosity can be seen in the fine porosity (for the sealing and the top coat), and the coarse porosity ranges due to the approach proposed in Section 2.3. The lowest porosity was observed in the SPS YSZ-M sample. Followed by the SPS GZO-M and SPS GZO-C sample, the difference between these two samples can be due to the higher porosity of the ceramic sealing layer compared to the metallic sealing layer. The highest porosity was observed in the SPS YSZ P-M due to the significantly high porosity of the top coat in this sample.

3.3. Thermal properties

Fig. 11 shows the thermal conductivity of the first and second architecture and Fig. 12 the third architecture samples, measured from 25 to 700 °C.

According to Fig. 11, the lowest thermal conductivity was observed for the APS sample, followed by the SPS GZO sample. The highest thermal conductivity values were observed in SPS YSZ samples with both thicknesses of top coats (SPS YSZ and SPS YSZ T).

Fig. 12 shows the thermal conductivity of the third architecture samples, where the lowest thermal conductivity was observed on the SPS GZO-C sample, followed by the SPS GZO-M sample. The SPS YSZ P-M sample and the SPS YSZ-M sample exhibited the highest thermal conductivity.

The thermal effusivity of the coatings was calculated and plotted in Figs. 13 and 14, based on the thermal conductivity values in the same temperature range. It can be observed that coatings' effusivity follow the same ranking as thermal conductivity.

In Fig. 13, the lowest thermal effusivity among the first and second architecture samples was revealed by the APS sample. The second-lowest thermal effusivity was shown by the SPS GZO sample, followed by the SPS YSZ sample, while the highest thermal effusivity was found for SPS YSZ T sample.

The thermal effusivity for the third architecture samples is shown in Fig. 14 with the lowest thermal effusivity for the SPS GZO-C sample, followed closely by the SPS GZO-M and successively the SPS YSZ P-M sample. The highest thermal effusivity was observed for the SPS YSZ-M sample.

3.4. Thermal cyclic fatigue test

SEM analysis of the cross-sectioned samples exposed to thermal cyclic fatigue (TCF) for 600 and 1000 cycles revealed that all coatings underwent failure at the edges due to the oxidation of the substrate. This trend became more noticeable as the test progressed, and the samples were exposed to more cycles, as shown in Fig. 15.

To better highlight the phenomenon related to the failure at the edges of the samples, higher magnification images were taken from the samples after 600 and 1000 cycles. The microstructure images of these samples are presented in Table 2 and 3.

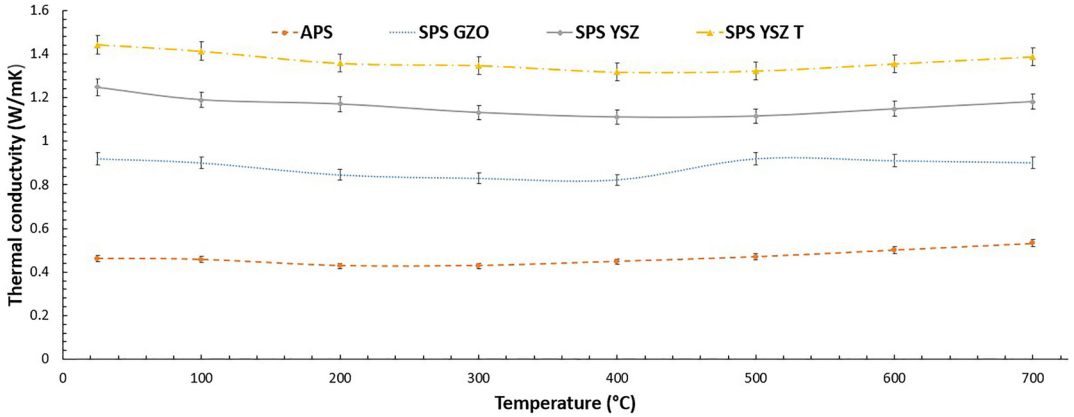

Fig. 11. Thermal conductivity along with the temperatures for the first and second architecture of top coated samples.

In Table 2, the results of the first and second architecture samples show that for the APS, SPS YSZ, and SPS YSZ T samples, the cracks originated at the bond coat/top coat interface and can be associated with the growth of oxides that formed on the substrate.

The cross-section micrographs of third architecture samples are shown in Table 3. The first observation is that the opening and widening of the cracks grew with the number of cycles and that cracks formed at the interface between top coat and bond coat oxides are grown inward on the substrate, same behavior shown in Table 2 for first and second architecture samples. A difference was remarked when metallic sealing layer samples were tested, e.g., SPS YSZ-M. In this case, a larger opening and widening of cracks could be observed.

3.5. Flame rig test

The flame rig test results of the samples with first and second architecture are shown in Fig. 16. The longest lifetime in this test was obtained by the SPS YSZ T sample, which showed no failure signs after 6000 cycles. The second-highest lifetime was observed for the SPS GZO sample followed by the thin SPS YSZ, while the APS sample exhibited the shortest lifetime.

The cross-section microstructures of the first and second architectures samples after testing are shown in Fig. 17. The APS coating delaminated, first near the interface between the bond coat and top coat due to cracking that extended through the topcoat until complete delamination. The second delaminated coating was the SPS YSZ; the reason for the failure could be the observed abrupt growth of a thick layer of oxide at the bond coat/substrate interface. The SPS YSZ T coating remained in good condition after testing without any failure after 6000 cycles. The SPS GZO sample failed revealing cracks at the top coat/bond coat interface and in the middle of the top coat.

The flame rig test results for the third architecture samples are shown in Fig. 18. It can be observed that all samples with metallic sealing layers failed after a few cycles, and the SPS GZO-C sample failed after around 4000 cycles on average. In Fig. 19, the cross-section microstructures of the third architectures after testing is shown, revealing a premature failure of the metallic sealing layer and the delamination of top coat in the ceramic sealing layer.

4. Discussion

4.1. Microstructure

Evaluating the main outcomes of using APS TBCs in diesel engines [5,13], the microstructural features of the best-reported work are similar to the APS used in this study, the first architecture. Both microstructures mainly consist of overlapped splats, creating a lamellar microstructure with cracks, pores, and oxides, both in the top coat and bond coat. Interlamellar cracks were mostly horizontally oriented, also identified as delaminations, providing good thermal insulation properties. In these APS coatings, cracks can relatively easily propagate due to the lamellar microstructure and the weak bonding between the splats. The high amount of interconnected pores (pore network) in APS TBCs allows the penetration of combustion gases during the compression stroke, and then during the exhaust stroke, due to the fast release of the pressure, the horizontal cracks could propagate leading to the delamination of the coating.

The column gaps, shown in the second and third architectures, when present in a large number, can generate a higher thermal conductivity, as shown by Carpio et al. [22], due to the creation of a lower

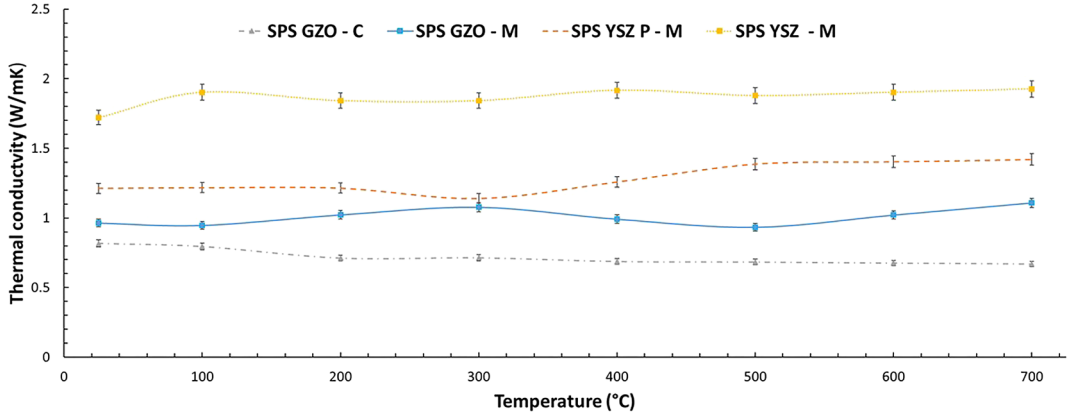

Fig. 12. Thermal conductivity along with the temperatures for the third architecture of top coated samples.

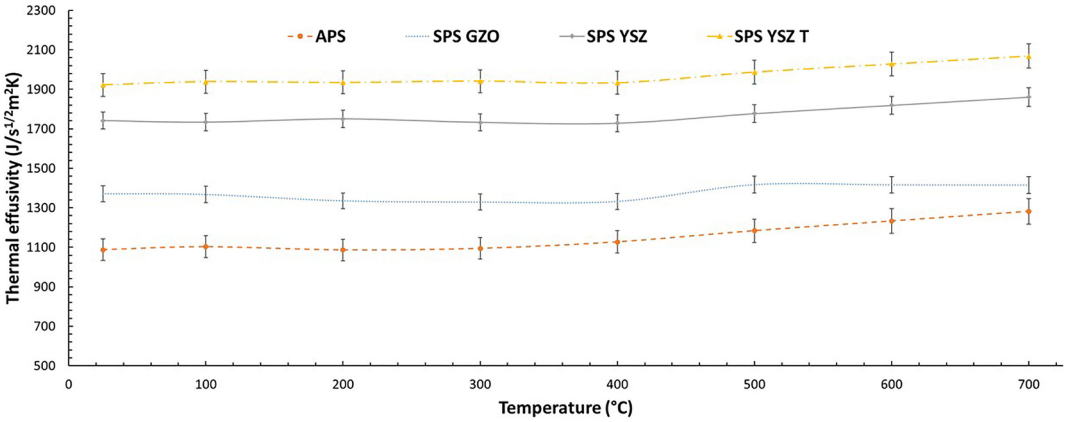

Fig. 13. Thermal effusivity along with the temperatures for the first and second architecture of top coated samples.

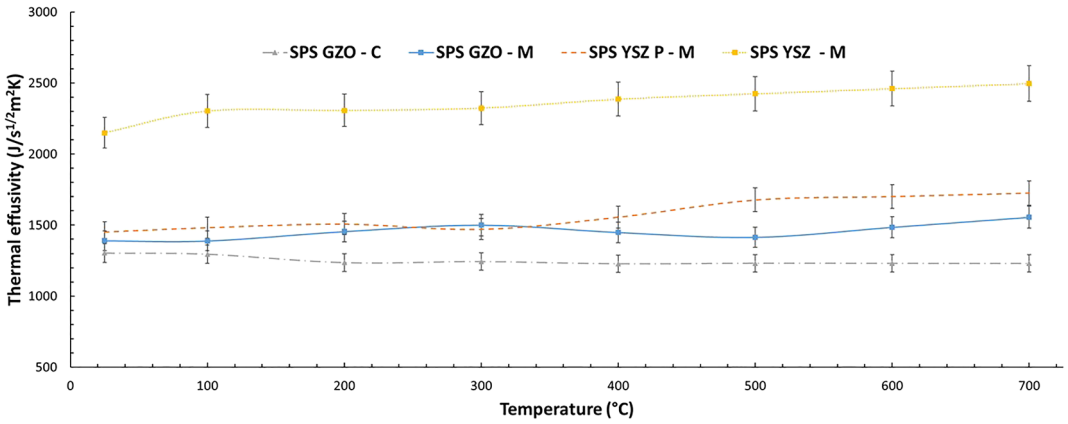

Fig. 14. Thermal effusivity along with the temperatures for the third architecture of top coated samples.

resistance path for the heat flow. These column gaps combined with the porosity in the columns and the pressure variation can, in the same way as in the APS, allow the infiltration of combustion gases and could lead to the coating failure. In this study, the sealing layers were used as an attempt to counteract this phenomenon.

On the third architecture, additionally was observed that the sealing layer followed the columnar profile of the top coats accurately without delamination or other types of defects that could grow and lead to failure during the service of the coating.

4.2. Porosity

The coating from the second and third architectures showed, in general, almost half of the porosity originating from the fine pores, highlighting the importance of the analysis at different magnifications but also the high content of small-scale porosity in SPS coatings. The coarse porosity also showed that it could be an influence on the total porosity, e.g., the sample SPS YSZ P-M. In this sample, the coarse porosity represented twice the amount of fine porosity.

The metallic sealing layer influenced the porosity on both fine, coarse, and total porosity. Samples containing a metallic sealing layer presented lower porosity than the samples without the metallic sealing layer, but if they are compared, disregarding the metallic sealing layer, the porosity should be similar.

The influence of the ceramic sealing layer on total porosity was not as strong as the metallic sealing layer due to its higher porosity, resulting in porosities on the same range of values as the sample without sealing layer.

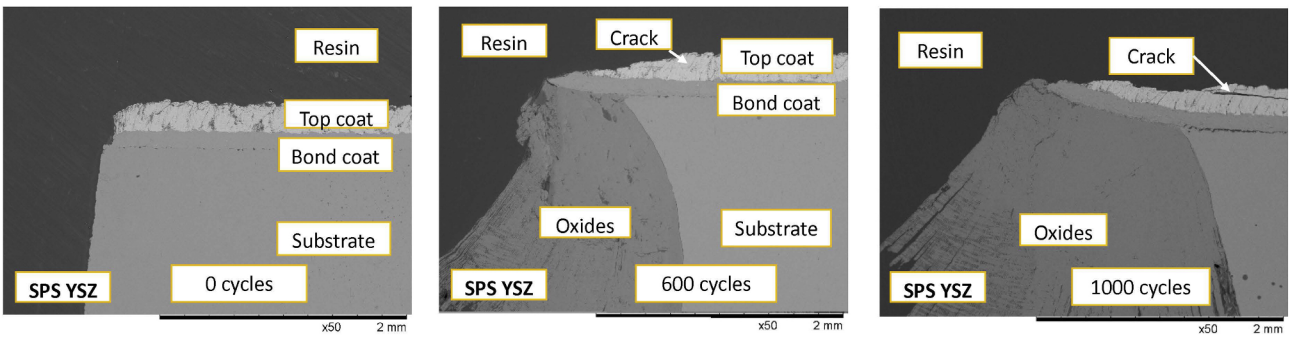

Fig. 15. Evolution of the thermal cyclic fatigue test for the sample SPS YSZ.

Table 2
Higher magnification of the failure in the first and second architecture top coated samples.

	600 cycles	1000 cycles
APS	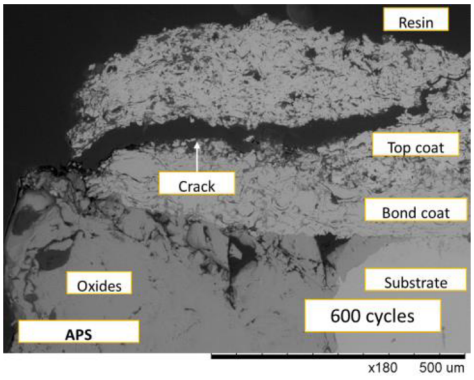	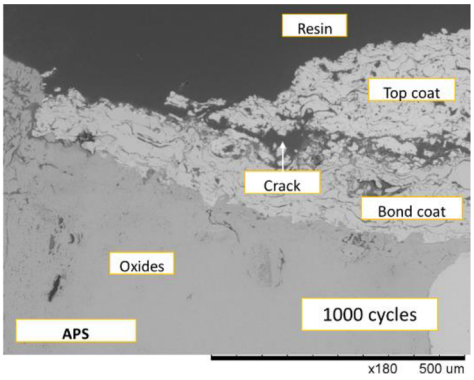
SPS YSZ	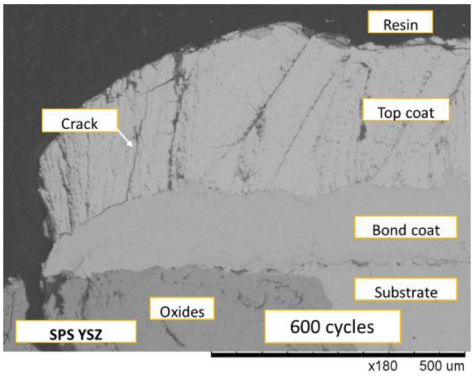	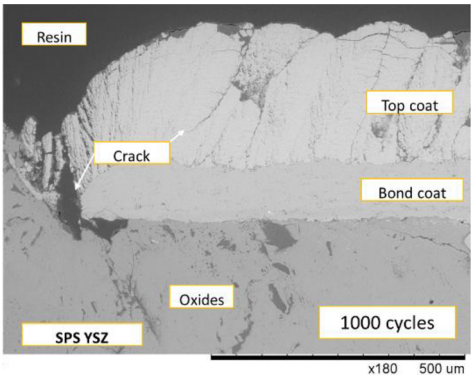
SPS YSZ T	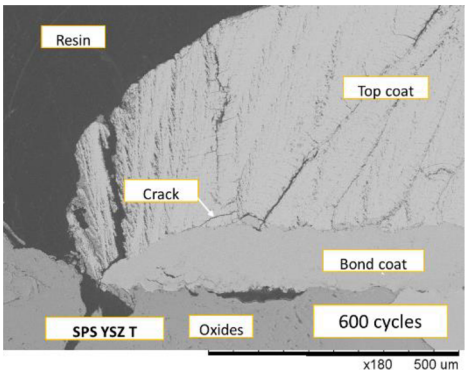	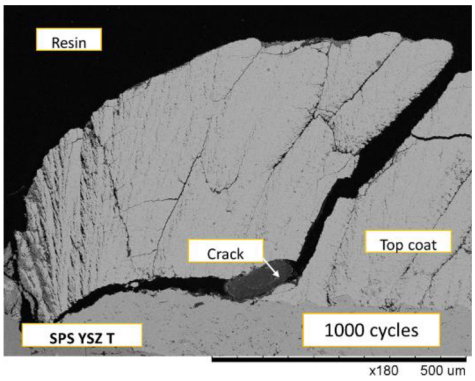
SPS GZO	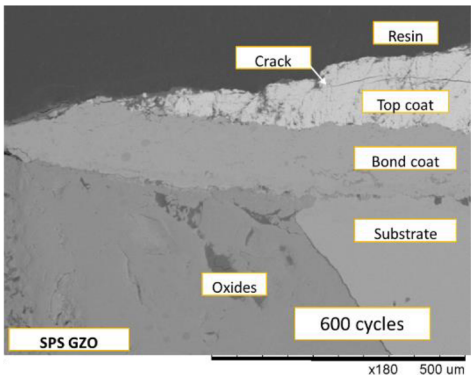	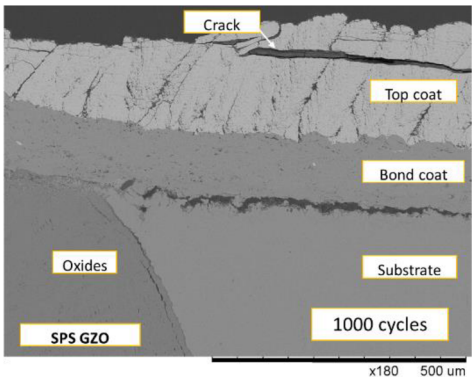

4.3. Thermal properties

As shown in Fig. 11, a slight decrease in thermal conductivity was observed with increasing the temperature until approximately 500 °C. Similar behavior was observed in the literature, and it is attributed to increased phonon scattering with increasing temperature [23–25]. Another observation in [23] and noted herein was that after 400 °C, the thermal conductivity of the samples increased, which could be attributed to the radiative mode of heat transfer.

For the first and second architecture, the lowest thermal conductivity was the APS coating with a lamellar microstructure, as presented in Section 3.1 where the cracks parallel to the surface led to a

Table 3
Higher magnification of the failure in the third architecture top coated samples.

	600 cycles	1000 cycles
SPS YSZ P-M	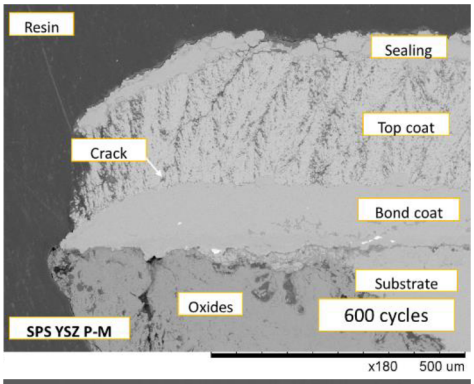	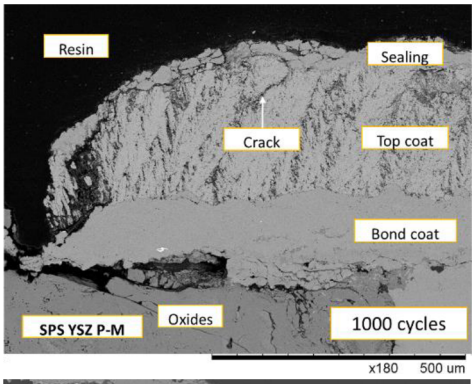
SPS YSZ -M	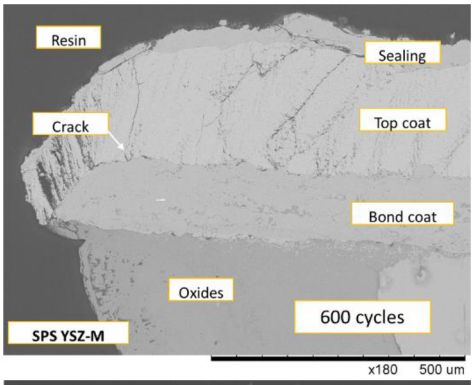	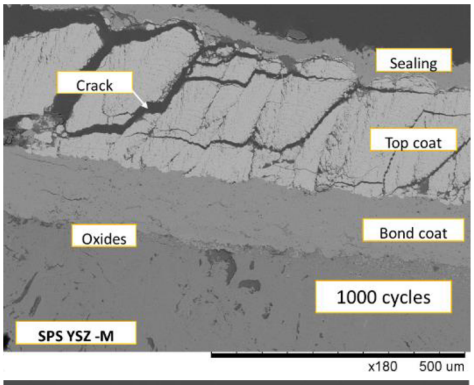
SPS GZO-C	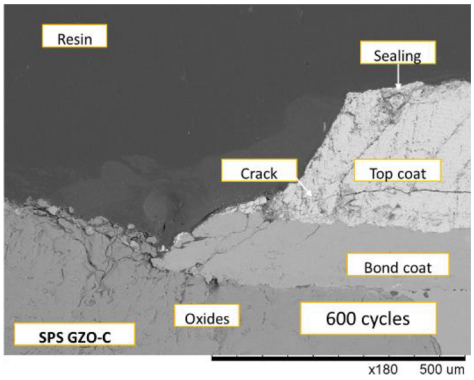	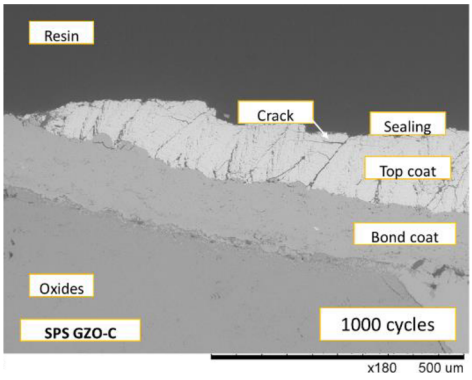
SPS GZO-M	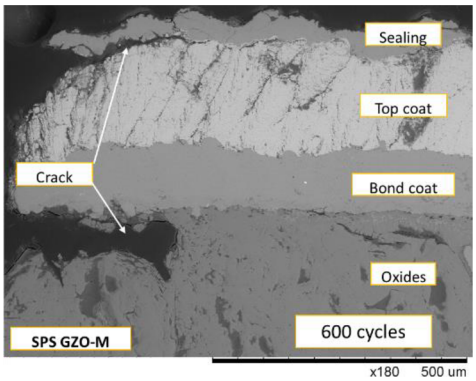	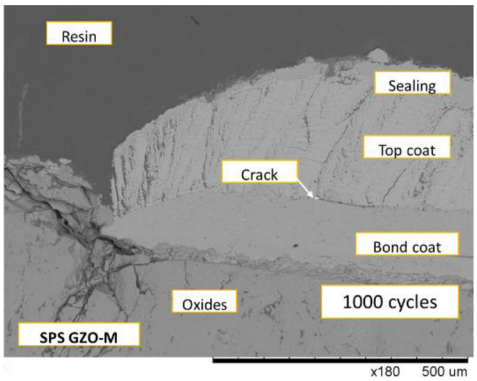

higher resistance path for the heat flow generating a lower thermal conductivity coating, a similar trend found by Refs. [25]. The following coating was the SPS GZO, which could be expected result since this material (GZO) has lower thermal conductivity in bulk compared to that of YSZ [17,26,27]. The similar values of thermal conductivity for the SPS YSZ and SPS YSZ T were also expected since the same spray parameters were used for producing them, and only the coating thickness was changed.

For the third architecture samples, no general increasing or decreasing trends were observed with increasing temperature (Fig. 12). The SPS GZO coating exhibited the lowest thermal conductivity among the SPS produced coatings. Thus, the expected behavior was observed

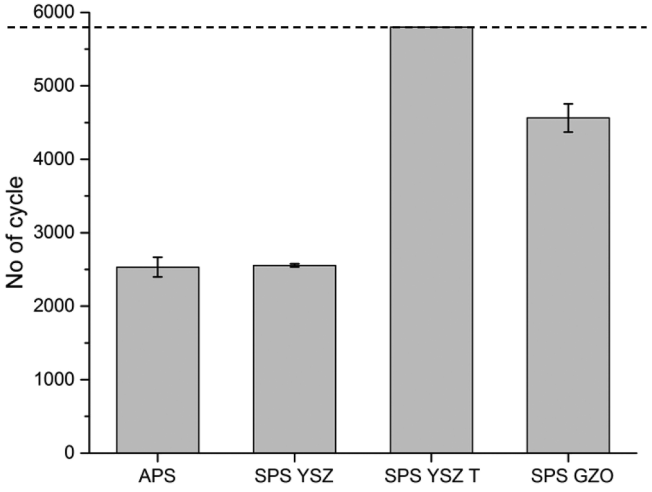

Fig. 16. Number of cycles for first and second architecture of top coat samples flame rig test.

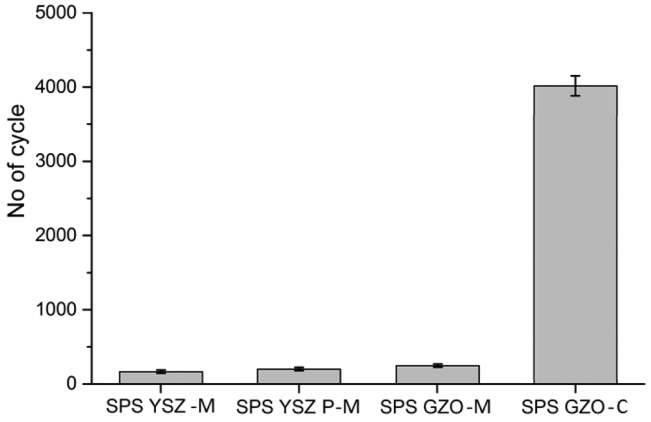

Fig. 18. Number of cycles for third architecture of top coated samples flame rig test.

even for the case of having a sealing layer. The underlying mechanism of the higher thermal conductivity for the metallic sealing layer is likely associated with the higher conductivity of metals compared to ceramics, which resulted in a lower thermal conductivity for the SPS GZO-C compare to the SPS GZO-M. In this way, an increase in the thermal conductivity was detected with the adding of the metallic sealing layer.

As described in Section 2.6 and Appendix A, the thermal effusivity is an excellent parameter that can be used to assess the thermal properties of coatings applied to diesel engine parts. This is because it takes into consideration the exchange of heat with the surroundings, giving in this way useful information for coatings to be investigated for automotive applications. The thermal effusivity results also corroborated with the thermal conductivity due to the similar ranking observed in almost all the samples.

4.4. Thermal cyclic fatigue

In this test, the typical failure mechanism for TBCs was not observed as the coatings did not detach from the bond coat, but the substrates underwent severe oxidation. These oxides grew, inwardly parallel to the layers and within the substrate, and became thick, i.e., > 2 mm leading to the failure only at the lateral edges of the coatings, while the

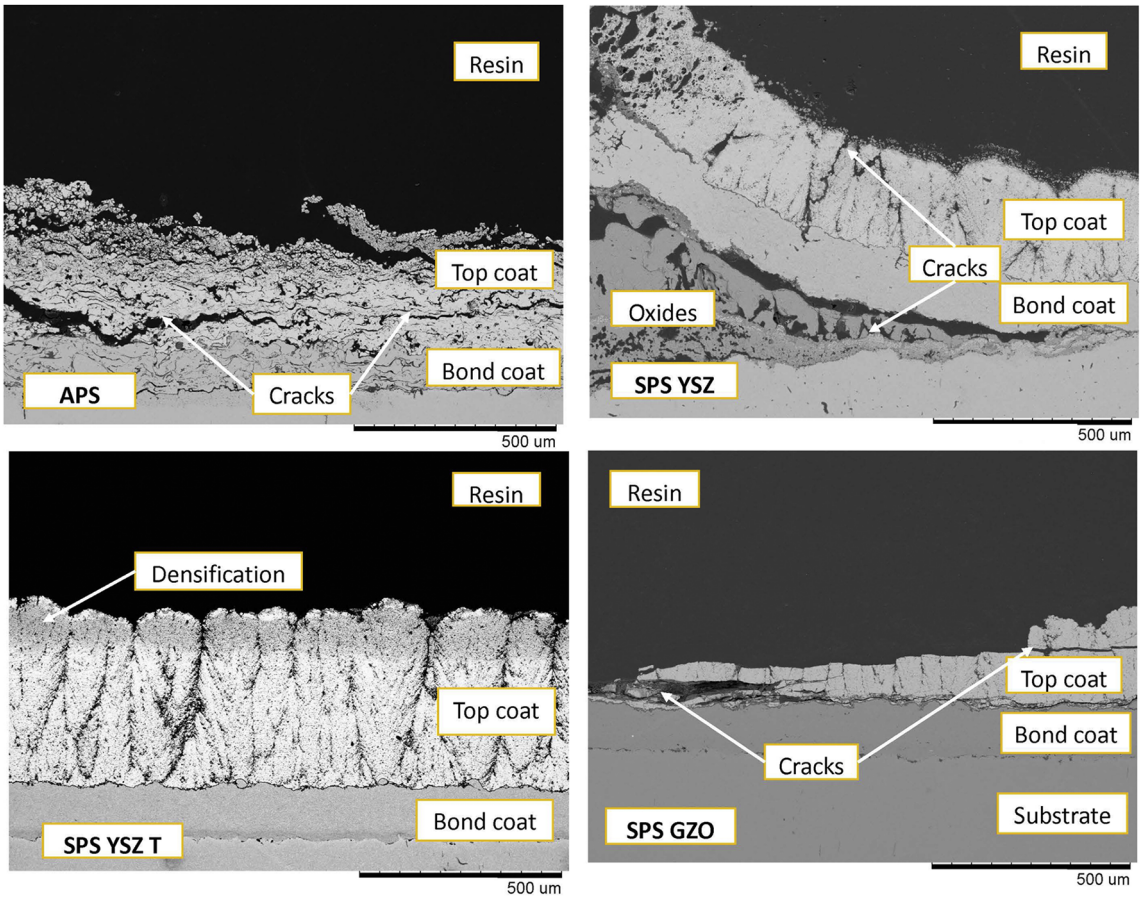

Fig. 17. Cross section of the first and second architecture of top coated samples after flame rig test.

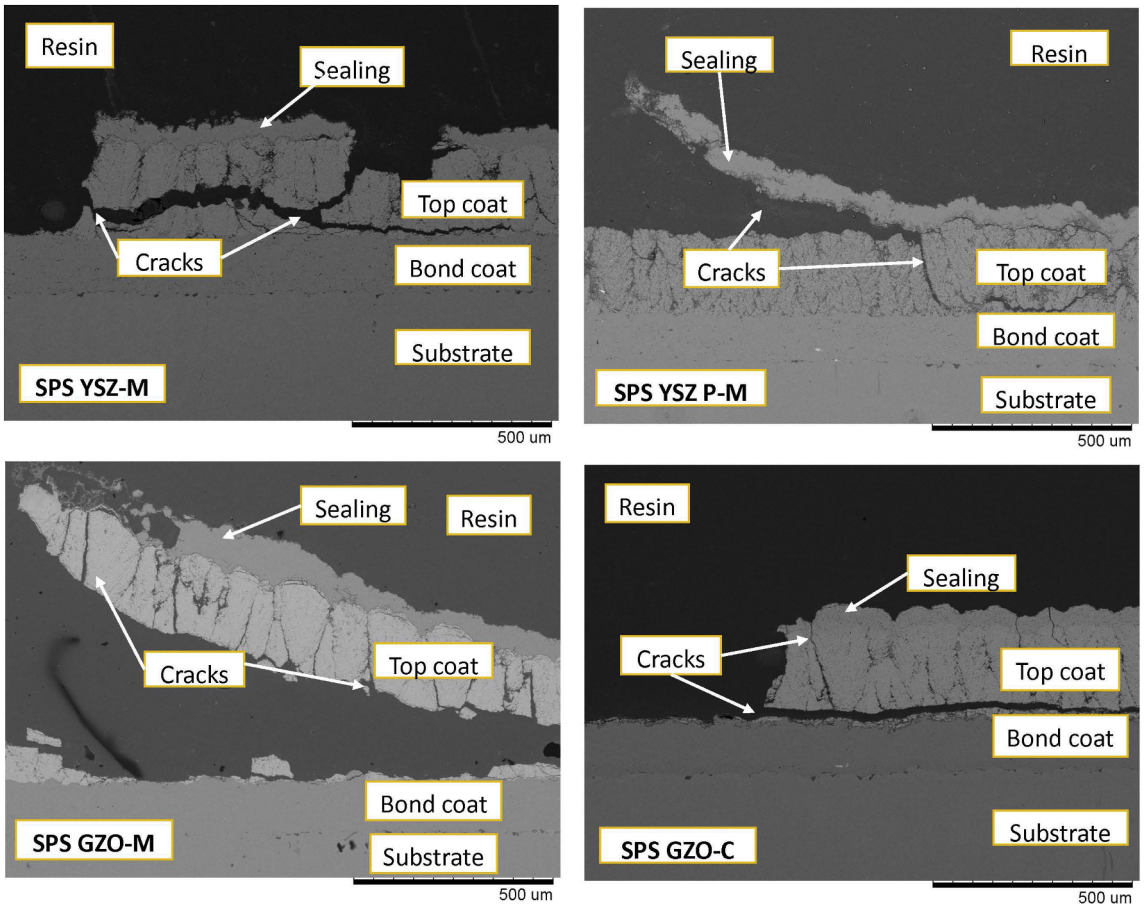

Fig. 19. Cross section of the third architecture of top coated samples after flame rig test.

rest of the sample remained intact during the whole test.

This happened due to the direct exposure of the metallic substrate on the sides to the hot atmosphere in the furnace during the thermal cycles, while the layers that protect against oxidation are only on the top where no oxidation was observed. This phenomenon can also happen in a real application as the piston edges are exposed to the combustion environment, and if this behavior continues, the piston can be scuffed.

4.5. Flame rig test

In the flame rig test, the longest lifetime of the SPS YSZ T sample may be due to the thickness of the top coat, which is the highest among all samples tested in this study. A thicker top coat results in a higher temperature drop across the coating, and thus the temperature at the bond coat/topcoat interface would be lower than in the lower thickness top coats, which could have contributed to the good performance of this sample in this test.

Comparing the samples with similar thicknesses of the top coat, e.g., between 200 μm and 300 μm, the SPS GZO sample showed the best results. This was likely due to the lower thermal conductivity of the SPS GZO, as shown in Section 3.3, compared to the SPS YSZ sample.

For the first architectures, the delamination may be due to the stresses that the sample encountered during the thermal cycling process, which, combined with the lamellar microstructure of the APS, facilitated the failure of the coating. In the second architecture, different behaviors were noticed; in the SPS YSZ sample, there was the formation of a thick layer of oxides in the interface between the substrate and the bond coat. This oxide layer induced high stress in the coating bending it. These stresses, combined with the stresses that come from thermal expansion mismatches between the ceramic top coat and the metallic bond coat, could have led to coating delamination from the substrate and the cracking on the top coat. Densification arose from sintering in the top coat closer to the surface in SPS YSZ T, as also observed in Ref. [3], which was likely due to cycling thermal exposure.

In the third architecture samples, the failure of the metallic sealing layer, as observed in Fig. 19, might be due to the rapid accumulation of a high amount of heat in the metallic layer, which could not be rapidly dissipated due to the low heat-conductive ceramic coating underneath. This effect was combined with uneven heat distribution due to the hot spot of the flame focused around the middle of the sample. This contributed to the rapid expansion (and even melting, in some cases) of the sealing layer followed by its detachment from the ceramic top coat as in sample SPS YSZ P-M or the extreme thermal stresses that lead to detachment of the top coat and sealing layer as for samples SPS YSZ-M and SPS GZO-M. In the ceramic sealing layer sample, the failure can come from the stresses induced by thermal cycling and the lower strain tolerance of the denser ceramic sealing layer. This result indicates that the ceramic sealing layer, despite a much better performance than the metallic sealing layer, could not exceed the performance of the second architecture samples. Further tests must be performed to replicate better the conditions inside of the diesel engine.

5. Conclusion

TBCs composed of different materials prepared by various processes, and with different architectures were studied and compared in terms of their thermal properties and lifetime in cyclic tests. The main conclusions can be summarized as follows:

- The lowest thermal effusivity for the first and second architecture samples was observed for the APS, followed by SPS GZO. For the third architecture samples, the lowest thermal effusivity was the SPS GZO-C, followed by SPS GZO-M and then SPS YSZ P-M. The thermal effusivity followed the same ranking as the thermal conductivity.
- The thermal cyclic fatigue test revealed that oxidation could be a problem for the coating if the uncoated regions in its nearby are not protected against oxidation. This result could be relevant for real applications as failure can occur at the edges of a piston coated with a TBC.
- The best performance in the flame rig test was displayed by the GZO SPS sample when compared to YSZ SPS and APS with similar thicknesses. Thus, the newly implemented SPS exhibited advantages over the reference APS method for internal combustion engines in terms of performance under thermal cyclic conditions.
- Although the TBCs were successfully sealed with dense metallic or ceramic sealing coatings, further tests need to be performed to assess their performance. The testing method perhaps needs further development to avoid high local heat concentration on the sample's surface.

Credit author statement

Research question and idea: Together with the supervisors, Wellington Uczak de Goes formulate the research question.

Literature review: Wellington Uczak de Goes performed the literature review. Robert Vaßen helped to formulate part of the discussions related to the thermal effusivity.

Experimental work: Wellington Uczak de Goes performed the experimental work with the help of lab engineers. Taishi Matsushita facilitated the process by allowing Wellington Uczak de Goes to use the Jönköping University flame rig test. The LFA measurements were performed by Ms. Kseniya Illkova.

Data analysis: Wellington Uczak de Goes performed the data analysis.

Interpretation of the results: Wellington Uczak de Goes interpreted the results. Other authors helped by giving valuable inputs.

Comparison with earlier research: The authors worked together in relating the findings with the earlier research.

Conclusion: Wellington Uczak de Goes proposed the conclusions based on the findings. Other authors reviewed, verified, and suggested necessary changes in the conclusions.

Manuscript writing: Wellington Uczak de Goes drafted the first version of the manuscript. Thereafter the manuscript was reviewed and edited by the other authors.

This is to certify that the authors are in agreement that the above mentioned description of contribution are truthfully and in line with common scientific code of conduct.

Declaration of competing interests

The authors declare that they have no known competing financial interests or personal relationships that could have appeared to influence the work reported in this paper.

Acknowledgments

The authors are gratefully acknowledging the Swedish Energy Agency for their support for this work, part of the FFI Energy & Environment Program. Authors also would like to thank Stefan Björklund from University West, Trollhättan, to help in planning the spray trials for all the samples and Adwait Jahagirdar for helping in preparing the samples.

Appendix A. Supplementary data

Supplementary data to this article can be found online at https://doi.org/10.1016/j.surfcoat.2020.125950.

References

[1] Sweden's Climate Act and Climate Policy Framework, Naturvardsverket, Stockholm, http://www.swedishepa.se/Environmental-objectives-and-cooperation/Swedish-environmental-work/Work-areas/Climate/Climate-Act-and-Climate-policy-framework-/, (2018) , Accessed date: 10 July 2019.
[2] Swedish Transport Administration Annual Report, Trafikverket, Borlänge, 2018, https://trafikverket.ineko.se/Files/sv-SE/49148/Ineko.Product.RelatedFiles/2018_086_TRV_Annual%20Report_2017.pdf, (2017) , Accessed date: 10 July 2019.
[3] M. Gupta, N. Markocsan, X.-H. Li, R.L. Peng, Improving the lifetime of suspension plasma sprayed thermal barrier coatings, Surf. Coat. Technol. 332 (2017) 550–559, https://doi.org/10.1016/j.surfcoat.2017.07.078.
[4] D.W. Parker, Thermal barrier coatings for gas turbines, automotive engines and diesel equipment, Mater. Des. 13 (1992) 345–351, https://doi.org/10.1016/0261-3069(92)90005-3.
[5] M.B. Beardsley, P.G. Happoldt, K.C. Kelley, E.F. Rejda, D.F. Socie, Thermal Barrier Coatings for Low Emission, High Efficiency Diesel Engine Applications, SAE International, 1999, https://doi.org/10.4271/1999-01-2255.
[6] D.R. Tree, D.C. Oren, T.M. Yonushonis, P.D. Wiczynski, Experimental Measurements on the Effect of Insulated Pistons on Engine Performance and Heat Transfer, SAE International, 1996, https://doi.org/10.4271/960317.
[7] R. Kamo, N.S. Mavinahally, L. Kamo, W. Bryzik, E.E. Schwartz, Injection Characteristics that Improve Performance of Ceramic Coated Diesel Engines, SAE International, 1999, https://doi.org/10.4271/1999-01-0972.
[8] A.J. Modi, Experimental Study of Energy Balance in Thermal Barrier Coated Diesel Engine, SAE International, 2012, https://doi.org/10.4271/2012-01-0389.
[9] A. Thibblin, S. Kianzad, S. Jonsson, U. Olofsson, Running-in behaviour of thermal barrier coatings in the combustion chamber of a diesel engine, Proc. Inst. Mech. Eng. D J. Automob. Eng. 234 (2019) 172–182, https://doi.org/10.1177/0954407019841173.
[10] H. Kosaka, Y. Wakisaka, Y. Nomura, Y. Hotta, M. Koike, K. Nakakita, A. Kawaguchi, Concept of “temperature swing heat insulation” in combustion chamber walls, and appropriate thermo-physical properties for heat insulation coat, SAE Int. J. Engines 6 (2013) 142–149, https://doi.org/10.4271/2013-01-0274.
[11] K. Osawa, R. Kamo, E. Valdmanis, Performance of Thin Thermal Barrier Coating on Small Aluminum Block Diesel Engine, SAE International, 1991, https://doi.org/10.4271/910461.
[12] A. Kawaguchi, H. Iguma, H. Yamashita, N. Takada, N. Nishikawa, C. Yamashita, Y. Wakisaka, K. Fukui, Thermo-Swing Wall Insulation Technology; — a Novel Heat Loss Reduction Approach on Engine Combustion Chamber, SAE International, 2016, https://doi.org/10.4271/2016-01-2333.
[13] W. Uczak de Goes, J. Somhorst, N. Markocsan, M. Gupta, K. Illkova, Suspension plasma-sprayed thermal barrier coatings for light-duty diesel engines, J. Therm. Spray Technol. 28 (2019) 1674–1687, https://doi.org/10.1007/s11666-019-00923-8.
[14] A. Thibblin, S. Jonsson, U. Olofsson, Influence of microstructure on thermal cycling lifetime and thermal insulation properties of yttria-stabilized zirconia thermal barrier coatings for diesel engine applications, Surf. Coat. Technol. 350 (2018) 1–11, https://doi.org/10.1016/j.surfcoat.2018.07.005.
[15] J. Somhorst, W. Uczak De Goes, M. Oevermann, M. Bovo, Experimental Evaluation of Novel Thermal Barrier Coatings in a Single Cylinder Light Duty Diesel Engine, SAE International, 2019, https://doi.org/10.4271/2019-24-0062.
[16] A. Ganvir, N. Curry, S. Björklund, N. Markocsan, P. Nylén, Characterization of microstructure and thermal properties of YSZ coatings obtained by axial suspension plasma spraying (ASPS), J. Therm. Spray Technol. 24 (2015) 1195–1204, https://doi.org/10.1007/s11666-015-0263-x.
[17] S. Mahade, N. Curry, S. Björklund, N. Markocsan, P. Nylén, R. Vaßen, Functional performance of Gd2Zr2O7/YSZ multi-layered thermal barrier coatings deposited by suspension plasma spray, Surf. Coat. Technol. 318 (2017) 208–216, https://doi.org/10.1016/j.surfcoat.2016.12.062.
[18] S. Akula Babuprakash, J. Jojo, Thermophysical and Mechanical Properties of TBC, Master Thesis Jönköping University, 2013.
[19] P. Fauchais, V. Rat, J.-F. Coudert, R. Etchart-Salas, G. Montavon, Operating parameters for suspension and solution plasma-spray coatings, Surf. Coat. Technol. 202 (2008) 4309–4317, https://doi.org/10.1016/j.surfcoat.2008.04.003.
[20] K. VanEvery, M.J.M. Krane, R.W. Trice, H. Wang, W. Porter, M. Besser, D. Sordelet, J. Ilavsky, J. Almer, Column formation in suspension plasma-sprayed coatings and resultant thermal properties, J. Therm. Spray Technol. 20 (2011) 817–828, https://doi.org/10.1007/s11666-011-9632-2.
[21] P. Fauchais, J. Heberlein, M. Boulos, Thermal Spray Fundamentals. From Powder to Part, (2013), https://doi.org/10.1007/978-0-387-68991-3.
[22] P. Carpio, Q. Blochet, B. Pateyron, L. Pawłowski, M.D. Salvador, A. Borrell, E. Sánchez, Correlation of thermal conductivity of suspension plasma sprayed yttria stabilized zirconia coatings with some microstructural effects, Mater. Lett. 107 (2013) 370–373, https://doi.org/10.1016/j.matlet.2013.06.051.
[23] S. Mahade, N. Curry, K.P. Jonnalagadda, R.L. Peng, N. Markocsan, P. Nylén, Influence of YSZ layer thickness on the durability of gadolinium zirconate/YSZ double-layered thermal barrier coatings produced by suspension plasma spray, Surf. Coat. Technol. 357 (2019) 456–465, https://doi.org/10.1016/j.surfcoat.2018.10.

046.
[24] J. Wu, X. Wei, N.P. Padture, P.G. Klemens, M. Gell, E. García, P. Miranzo, M.I. Osendi, Low-thermal-conductivity rare-earth zirconates for potential thermal-barrier-coating applications, J. Am. Ceram. Soc. 85 (2002) 3031–3035, https://doi.org/10.1111/j.1151-2916.2002.tb00574.x.
[25] D.R. Clarke, Materials selection guidelines for low thermal conductivity thermal barrier coatings, Surf. Coat. Technol. 163–164 (2003) 67–74, https://doi.org/10.1016/S0257-8972(02)00593-5.
[26] Y. Wang, H. Liu, X. Ling, Y. Weng, Effects of pore microstructure on the effective thermal conductivity of thermal barrier coatings, Appl. Therm. Eng. 102 (2016) 234–242, https://doi.org/10.1016/j.applthermaleng.2016.03.174.
[27] N. Curry, N. Markocsan, X.-H. Li, A. Tricoire, M. Dorfman, Next generation thermal barrier coatings for the gas turbine industry, J. Therm. Spray Technol. 20 (2011) 108–115, https://doi.org/10.1007/s11666-010-9593-x.